Spin-dependent transport and current-induced spin transfer torque in a strained graphene spin valve

Kai-He Ding,[1,*] Zhen-Gang Zhu,[2,3,†] and Gang Su[2,‡]

[1]*Department of Physics and Electronic Science, Changsha University of Science and Technology, Changsha 410076, China*

[2]*Theoretical Condensed Matter Physics and Computational Materials Physics Laboratory, School of Physics, University of Chinese Academy of Science, Beijing 100049, China*

[3]*School of Electronic, Electrical and Communication Engineering, University of Chinese Academy of Sciences, Beijing 100049, China*

(Received 7 March 2014; published 27 May 2014)

Using the nonequilibrium Green's function method, we investigated theoretically the spin-dependent transport and the current-induced spin transfer torque (CISTT) in a zigzag-graphene-nanoribbon (ZGNR) spin valve in the presence of an applied uniaxial strain to the ZGNR. It is found that, when a longitudinal or transverse strain is applied, the conductance versus the Fermi energy remains unchanged around the Dirac point. However, when the Fermi energy is larger than the molecular field of two ferromagnetic electrodes, the dependence of the conductance on the uniaxial strain exhibits totally different behaviors for parallel and antiparallel configurations for the electrodes' magnetizations, which leads to a transition of magnetoresistance (MR) from a perfect histogramlike behavior to successive cusplike peaks and to a steplike behavior with sharp peaks for the longitudinal and transverse strains, respectively. It is further shown that the CISTT per unit of the bias voltage as a function of the Fermi energy is antisymmetric respective to the Dirac point and exhibits typical successive oscillations composed of broad peaks closely followed by sharp ones.

DOI: 10.1103/PhysRevB.89.195443 PACS number(s): 62.20.−x, 72.80.Vp, 75.47.−m

I. INTRODUCTION

Graphene, a single layer of carbon, was first fabricated as a perfect two-dimensional material in 2004 [1]. Its specific honeycomb structure is expected to be a host of many intriguing electronic properties such as the anomalous quantized Hall effect [2,3], the high electron mobility [1,4], as well as the long spin relaxation length [5], which underlines remarkably potential applications of graphene in spintronics [6]. Moreover, much attention has been paid to the investigation on the spin injection into graphene [7,8], magnetoresistance (MR) [9–12], current-induced spin transfer torque (CISTT) [13], and spin filtering effect [14–16] in various graphene-based devices, etc.

A merit of graphene is that its electronic properties can be tailored by means of a number of methods such as adatoms, defects, and external strains. Among them, strain is a particular way in regulating the electronic properties of graphene [17]. A considerable body of research has shown that the strain may induce a strong pseudomagnetic field in graphene [18–21], and leads to many fascinating behaviors in optical properties [22,23], specific heat [24], and plasmon excitations [25]. Moreover, there is still a great interest in exploring whether the strain is capable of manipulating the transport behavior in graphene-based nanoelectronic devices.

In this work we investigate theoretically the effect of strain on the spin-dependent transport and CISTT in a zigzag-edged-graphene-nanoribbon spin-valve device, where a uniaxial strain is exerted to the graphene sheet. By utilizing the nonequilibrium Green's function approach (e.g., Refs. [26,27]), we find that the conductance versus the Fermi energy exhibits successive steplike behavior. When a longitudinal (parallel to the x axis) or transverse strain (perpendicular to the x axis) is applied, the conductance almost remains intact for the Fermi energy lying around the Dirac point. However, when the Fermi energy is larger than the molecular field of the ferromagnetic (FM) electrodes, depending on the orientation of the applied strain, the width of each plateau of the conductance may increase or decrease upon increasing the strain for the antiparallel configuration of magnetization of the two FM electrodes; in contrast, for the parallel configuration of magnetization of both electrodes, the even (odd) plateaus of the conductance shrink, while odd (even) plateaus almost remain unchanged when the longitudinal (transverse) strain is applied. This result eventually leads to a transition of MR from a perfect histogramlike behavior to the successive cusp peaks for a longitudinal strain, or to the steplike behavior with sharp peaks for a transverse strain. We also show that the CISTT per unit of the bias voltage as a function of the Fermi energy exhibits a successive oscillation structure with a broad peak closely followed by a sharp one. Especially, an applied strain may significantly influence the spin-dependent scattering in the graphene spin-valve device, which will strongly modulate the variation of the CISTT with the Fermi energy.

II. THEORETICAL MODEL

We consider a zigzag-edged-graphene nanoribbon (ZGNR) whose two ends are placed under two FM electrodes, forming a spin-valve device, as shown in Fig. 1(a). Owing to the existence of FM electrodes, the ZGNR is divided into three regions: a central normal graphene strip and two FM polarized graphene ribbons. If the central region has the width N and length L, then it contains $N(2L+1)$ carbon atoms. A uniform uniaxial strain is applied to the ZGNR [see Fig. 1(b)]. The total Hamiltonian of the spin-valve system is given by

$$H = H_L + H_R + H_C + H_T, \tag{1}$$

*dingkaih@mails.ucas.ac.cn
†zgzhu@ucas.ac.cn
‡gsu@ucas.ac.cn

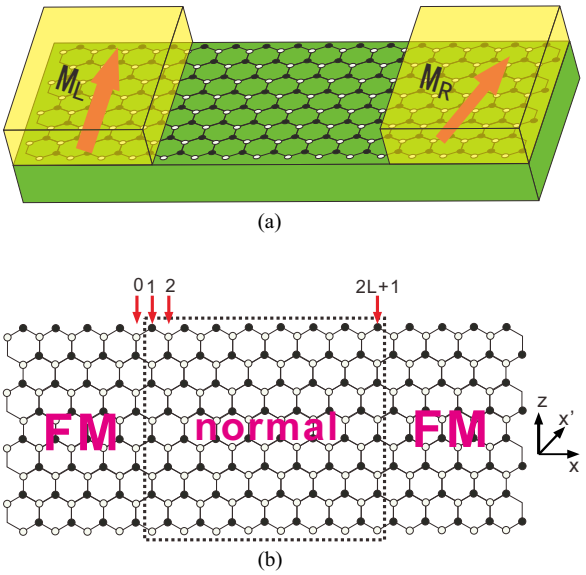

FIG. 1. (Color online) (a) A schematic depiction of the graphene-based spin-valve device. The zigzag-edged-graphene nanoribbon (ZGNR) is connected to two ferromagnetic electrodes (yellow). The magnetizations of two electrodes (red arrows) are aligned by a relative angle φ. (b) Schematic illustration showing the ZGNR divided into three regions by the ferromagnetic electrodes. The strain is applied to the ZGNR in the x' direction deviating by an angle θ from the x axis that defines the zigzag direction of the honeycomb lattice.

where H_L (H_R) describes the left (right) FM electrode, H_C is the Hamiltonian of the central graphene region, and H_T describes the coupling between the FM electrodes and central graphene. In the tight binding representation, H_L, H_R, H_C, and H_T can be written as

$$H_L = \sum_{i\in L,\sigma}(E_L + \sigma M_L)a^\dagger_{i\sigma}a_{i\sigma} - \sum_{i,i+\alpha\in L,\sigma}(t_\alpha a^\dagger_{i\sigma}a_{i+\alpha\sigma} + \text{H.c.}), \tag{2}$$

$$H_R = \sum_{i\in R,\sigma}[(E_R + \sigma M_R\cos\varphi)a^\dagger_{i\sigma}a_{i\sigma} + M_R\sin\varphi a^\dagger_{i\sigma}a_{i\bar{\sigma}}] - \sum_{i,i+\alpha\in R,\sigma}(t_\alpha a^\dagger_{i\sigma}a_{i+\alpha\sigma} + \text{H.c.}), \tag{3}$$

$$H_C = \sum_{i\in C,\sigma}E_C a^\dagger_{i\sigma}a_{i\sigma} - \sum_{i,i+\alpha\in C,\sigma}(t_\alpha a^\dagger_{i\sigma}a_{i+\alpha\sigma} + \text{H.c.}), \tag{4}$$

$$H_T = -\sum_{i\in C,i+\alpha\in L,R,\sigma}(t_\alpha a^\dagger_{i\sigma}a_{i+\alpha\sigma} + \text{H.c.}), \tag{5}$$

where E_L, E_R, and E_C are the on-site energies in the left, right, and central graphene, respectively, which can be tuned by the gate voltage, $a^\dagger_{i\sigma}$ ($a_{i\sigma}$) creates (annihilates) an electron with spin σ at site i, M_L and M_R are the magnetizations of the left and right FM electrodes, and φ is the angle between the orientations of M_L and M_R. When the strain is exerted to the graphene layer, the hopping matrix element is modified as $t_\alpha = t_0 e^{-3.37(|\mathbf{d}_\alpha|/a_0-1)}$ [28], $t_0 = 2.7$ eV, and $\mathbf{d}_\alpha$ ($\alpha = 1,2,3$) is the strained nearest neighbor vector [28] given by

$$\mathbf{d}_\alpha = (1+\varepsilon)\boldsymbol{\delta}_\alpha, \tag{6}$$

where $\boldsymbol{\delta}_1 = a_0(\sqrt{3}/2, -1/2)$, $\boldsymbol{\delta}_2 = a_0(0,1)$, $\boldsymbol{\delta}_3 = a_0(-\sqrt{3}/2, -1/2)$, $a_0 \approx 1.42$ Å being the carbon-carbon distance [17]

$$\varepsilon = \varepsilon_0\begin{pmatrix}\cos^2\theta - \sigma\sin^2\theta & (1+\sigma)\cos\theta\sin\theta \\ (1+\sigma)\cos\theta\sin\theta & \sin^2\theta - \sigma\cos^2\theta\end{pmatrix}, \tag{7}$$

with ε_0 being the strain modulus, and σ being the Poisson's ratio.

By using the nonequilibrium Green's function method [26,27], the electric current flowing through the system can be expressed by [29]

$$I = \frac{e}{h}\int d\varepsilon T_{LR}(\varepsilon)[f_L(\varepsilon) - f_R(\varepsilon)], \tag{8}$$

where f_λ ($\lambda = L, R$) is the Fermi distribution function for the λ electrode, and the transmission coefficient $T_{LR}(\varepsilon) = \text{Tr}[\Gamma_L(\varepsilon)G^r(\varepsilon)\Gamma_R(\varepsilon)G^a(\varepsilon)]$ with the linewidth function $\Gamma_\lambda(\varepsilon) = i[\Sigma^r_\lambda(\varepsilon) - \Sigma^a_\lambda(\varepsilon)]$ and Green's function $G^r(\varepsilon) = [G^a(\varepsilon)]^\dagger = 1/[\varepsilon - H_c - \Sigma^r_L(\varepsilon) - \Sigma^r_R(\varepsilon)]$. The retarded (advanced) self-energy $\Sigma^{r(a)}_\lambda(\varepsilon)$ can be obtained by solving the surface Green's function for the λ electrode [30,31]. After obtaining the electric current, the conductance can be calculated by $G = \partial I/\partial V$. For a small bias voltage, the conductance at zero temperature becomes

$$G = \frac{e^2}{h}T_{LR}(E_F), \tag{9}$$

where E_F is the Fermi energy. In terms of the result of Eq. (9), the MR can be obtained according to the conventional definition

$$MR = \frac{G(0) - G(\pi)}{G(0)}, \tag{10}$$

where $G(0) = G(\varphi = 0)$ [$G(\pi) = G(\varphi = \pi)$] is the conductance for the parallel (antiparallel) configuration of magnetizations of both electrodes.

When noncollinear configuration of the magnetizations is present (the magnetizations of the left and right electrodes are not parallel or antiparallel, but deviate from each other by an angle φ), a spin torque will be generated to the right ferromagnet by the spin-polarized current through the system and is called CISTT [32]. The so-called CISTT can be derived by calculating the time evolution rate of total spin in the right ferromagnetic electrode. By means of the nonequilibrium Green's function method, one can finally obtain [33,34]

$$\tau^{Rx} = \frac{1}{4\pi}\text{Tr}\int d\varepsilon[G^r(\varepsilon)\Gamma_L(\varepsilon)G^a(\varepsilon)\Gamma_R(\varepsilon)] \times(\sigma_x\cos\varphi - \sigma_z\sin\varphi)[f_L(\varepsilon) - f_R(\varepsilon)], \tag{11}$$

where σ_x and σ_z are the Pauli matrices.

III. BAND STRUCTURE OF STRAINED ZIGZAG-EDGED-GRAPHENE NANORIBBON

In order to analyze the effect of the strain on the spin-dependent transport through the graphene spin-valve device, we first calculate the band structure of the ZGNR in the

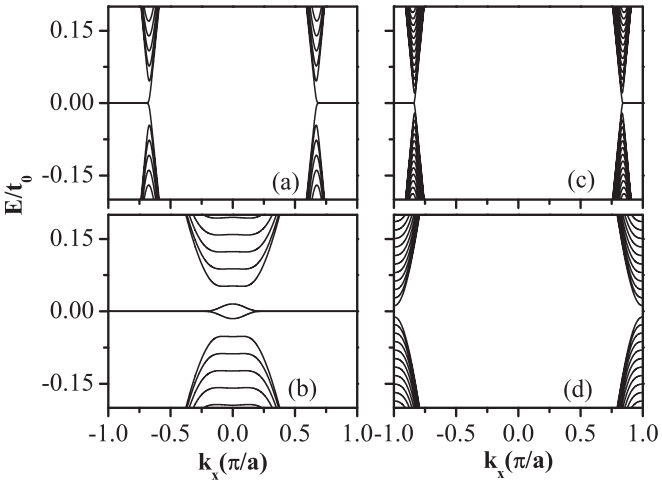

FIG. 2. The band structure of the strained graphene ribbons with zigzag edge. (a) $\varepsilon_0 = 0$; (b) $\varepsilon_0 = 0.23, \theta = 0$; (c) $\varepsilon_0 = 0.23, \theta = \pi/2$; and (d) $\varepsilon_0 = 0.23$, $\theta = \pi/3$, where $N = 100$, $a = \sqrt{3}a_0$, and L is infinite.

presence of a uniaxial strain. Throughout this paper we choose t_0 as a unit of energy.

Figure 2 shows the band structure of the ZGNR, which consists of two well-separated valleys K and K' located at the corners of the first Brillouin zone [except Fig. 2(b)]. The localized edge states form a pair of partial flat bands within the region of $2\pi/3 \leqslant |k_x a| \leqslant \pi$ in the absence of the strain, which is in agreement with the previous results [35,36]. When the longitudinal strain is applied, the two valleys approach each other with increasing the strain [see Fig. 2(b)], and eventually merge into a broad valley for a sufficiently strong strain. For a transverse strain case, the interval of the two valleys becomes wider [see Fig. 2(c)]. These results are reminiscent of the behaviors of bulk graphene [28]. However, from Figs. 2(b) and 2(d) one can find a notable difference in the dependence on the strain strength and direction between the band structures of the graphene nanoribbon and bulk graphene. For the latter, the strains along $\theta = 0$ and $\theta = \pi/3$ are most effective in overcoming the gap threshold [28]. Whereas for the graphene ribbon, the influence of the strain reveals different features due to one-dimensional confinement, i.e., for the longitudinal strain ($\theta = 0$), a gap is opened between the edge band and the first subband. The degenerate features of the edge bands always remain unchanged even for the deformation beyond 20%. When the strain direction is tuned to $\theta = \pi/3$, the flat edge band is driven to cross the boundary of the Brillouin zone under a large strain, and a gap between the edge bands appears. Thus, $\theta = \pi/3$ is the optimal direction in opening the band gap of the graphene ribbon with zigzag edges.

Furthermore, by comparing Figs. 2(b) and 2(c), it is interesting to note that the interval between the subbands becomes wider when the longitudinal strain is applied; while it shrinks for the transverse strain ($\theta = \pi/2$), as observed in Fig. 2(c). To understand this behavior, we could view the graphene ribbon as an effective coupling system consisting of many carbon chains along the x direction. The longitudinal (transverse) strain tends to enhance (suppress) the bond t_2 between the nearest neighbor carbon chains, thus leading to an increase (a decrease) of the subband splitting for these carbon chains.

IV. STRAIN DEPENDENCE OF CONDUCTANCE

Next, we study how the spin-dependent transport through the graphene spin-valve device is affected by the strain. For simplicity we assume that the two electrodes are made of the same material, i.e., $M_L = M_R = M$, and take the temperature to be zero and the on-site energies $E_L = E_R = E_C = 0$.

Figures 3(b) and 3(e) show the dependence of the conductance on the Fermi energy for parallel and antiparallel configurations of magnetizations in the absence of the strain. For $|E_F| < M$, the conductance versus E_F exhibits an oscillation behavior for the parallel configuration [see Fig. 3(b)]. This oscillation stems from scattering in a spin-down channel due to a mismatch between the parity of the transverse wave function in the central region and that of the left and right electrodes [11]. This is quite different from the case of the antiparallel configuration, in which the conductance displays a zero value plateau [see Fig. 3(e)]. This discrepancy can be understood by the combined effect of the spin-dependent scattering and band selective filter in a ZGNR [11]. When $|E_F| > M$, the conductance versus E_F in the parallel and

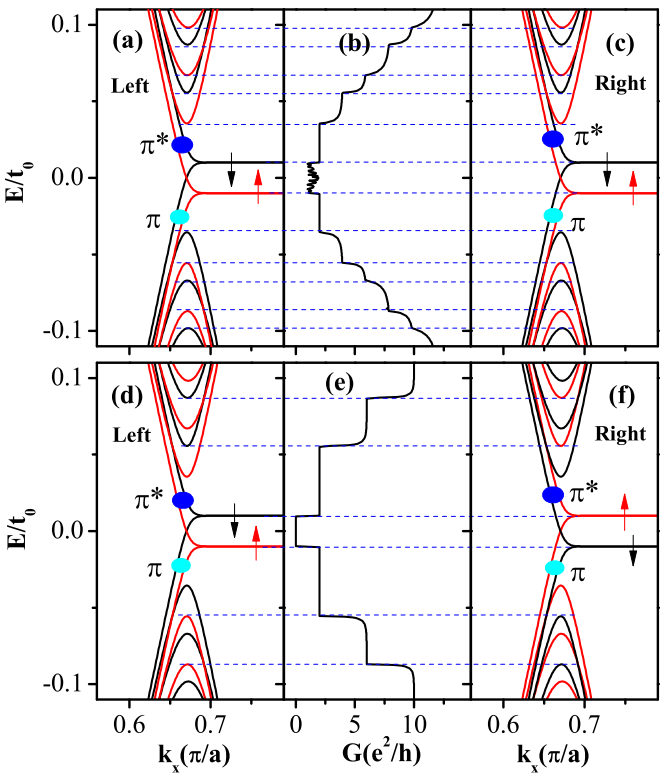

FIG. 3. (Color online) The conductance as a function of Fermi energy in (b) parallel and (e) antiparallel configurations of magnetization of two ferromagnetic electrodes in the absence of a strain. The corresponding band structures of the left and right spin-polarized ZGNR electrodes are also presented in (a) and (c) for parallel and (d) and (f) for antiparallel configuration, respectively. The arrows indicate the spin directions of electrons in the ferromagnetic electrodes. The parameters are taken as $N = 100, L = 20, M = 0.01$.

antiparallel configurations exhibits a steplike structure [37]. In order to understand this feature, we plot the band structures of the left and right ferromagnetic electrodes in Figs. 3(a), 3(d), 3(c), and 3(f). For the ZGNR, a reflection through a mirror plane (perpendicular to the graphene layer) located at the middle of the ribbon along the x direction gives rise to symmetric (π) and antisymmetric (π^*) characters of parity. If an electron coming from a state with the symmetric parity of the left electrode travels into a state with antisymmetric parity of the right electrode, it cannot be accommodated by this state of the right electrode. Therefore, the conductance in this case will be zero. This is the so-called parity selective transport [37,38]. When the ferromagnetic electrodes are introduced, the spin selective transport will be involved as well. Evidently, owing to the existence of the magnetization, the energy band n of the left and right electrodes is split due to the Zeeman effect as the spin subbands $n_\uparrow$ and $n_\downarrow$ [39]. The spin-up subbands $n_\uparrow$ shift relative to the spin-down ones $n_\downarrow$ by $2M$. For the parallel configuration, when the Fermi energy sweeps each spin subband n_σ ($\sigma = \uparrow, \downarrow$), a plateau in the conductance appears whose width Δ^P equals to $\Delta^P_{n\uparrow} = E_{n\uparrow} - E_{n-1\downarrow}$ or $\Delta^P_{n\downarrow} = E_{n\downarrow} - E_{n\uparrow} = 2M$, where $E_{n\sigma}$ is the energy of the spin subbands n_σ [see Fig. 3(b)].

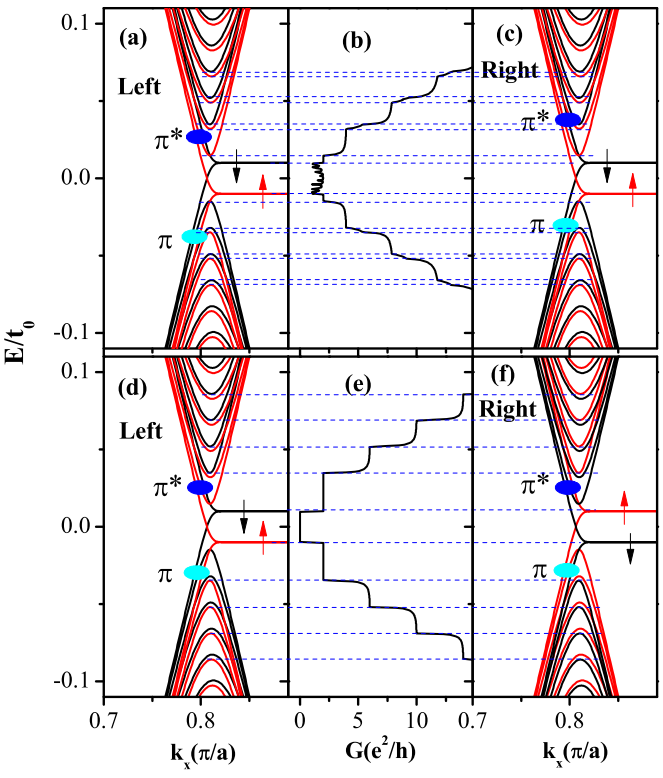

FIG. 4. (Color online) The conductance as a function of Fermi energy in (b) parallel and (e) antiparallel configurations of magnetization of two ferromagnetic electrodes in the presence of transverse strain ($\theta = \pi/2$) with $\varepsilon_0 = 0.18$. The corresponding band structures of the left and right spin-polarized ZGNR electrodes are also presented in (a) and (c) for parallel and (d) and (f) for antiparallel configuration, respectively. The arrows indicate the spin directions of electrons in the ferromagnetic electrodes. The other parameters are taken as the same as those of Fig. 3.

To analyze the selective transport we use [$L(R)$, n, $\uparrow$ ($\downarrow$), $\pi(\pi^*)$] to indicate the states of the left (right) electrode, nth subband, up (down) spin, and parity π (π^*), respectively. For the zero conductance plateau, the states of the left electrode are (L,0, $\uparrow$,π^*) and (L,-1, $\downarrow$,π), and the states of the right electrode are (R,-1, $\uparrow$,π) and (L,0, $\downarrow$,π^*). Therefore, there is no an opening channel between the left and the right electrodes because the spin and parity are not compatible. For the first conductance plateau ($2e^2/h$ at the positive energy side), the channels of (L,0, $\uparrow$,π^*) $\rightarrow$ (R,0, $\uparrow$,π^*) and (L,0, $\downarrow$,π^*) $\rightarrow$ (R,0, $\downarrow$,π^*) can open. The width of plateau for the antiparallel configuration is given by $\Delta^A_n = E_{n\downarrow} - E_{n-1\downarrow} = 2M + \Delta^P_{n\uparrow}$ [Fig. 3(e)].

When a transverse strain is applied, the conductance in the region $|E_F| < M$ almost remains intact, as shown in Figs. 4(b) and 4(e). However, the width of each plateau in the conductance at $|E_F| > M$ decreases for the antiparallel configuration when the transverse strain is applied [Fig. 4(e)]. This behavior is very different from the case of parallel configuration, where one can find that the odd plateaus of the conductance shrink, but the even ones almost remain unchanged for the transverse strain [Fig. 4(b)]. The reason is that when the transverse strain is taken into account, the interval between the subbands $E_{n\uparrow}$ and $E_{n-1\downarrow}$ becomes narrower [Fig. 2(c) or 4(d)], leading to the attenuation of the plateau width Δ^A_n in the conductance for antiparallel configuration. For the parallel configuration, the conductance contains two types of width of $\Delta^P_{n\uparrow}$ and $\Delta^P_{n\downarrow}$ plateaus, which correspond, respectively, to the odd and even plateaus of the conductance. Though the interval between the subbands $n_\uparrow$ and $(n-1)_\downarrow$ decreases with increasing the transverse strain strength ε_0, the separation between the pair of the spin-split subbands $n_\uparrow$ and $n_\downarrow$ is fixed for a given magnetization M. Furthermore, the spin-up and spin-down electrons contribute equally to the conductance, which, therefore, brings about a different dependence of the odd and even plateaus of the conductance on the strain strength for the parallel configuration.

When the longitudinal strain is applied, the conductance exhibits a completely different behavior from the case of the transverse strain. Close to the zero energy point, the spin-up (down) subbands of the two electrodes at the low energy are pushed down (up) across the $E = 0$ level in the parallel configuration. In this case, the combinations of the spin-dependent scattering and band selective filter lead to successive oscillations in the conductance versus Fermi energy in low energy region $|E_F| < M$ [11]. The oscillation persists even in the presence of the strain. However, the amplitudes of the oscillation peaks are suppressed and the positions of peaks are slightly moved due to the weakened bonds t_1 and t_3 by this longitudinal strain. It is further observed that the width of each plateau in the conductance for the antiparallel configuration at $|E_F| > M$ increases with increasing ε_0 [Fig. 5(b)]. In contrast, for the parallel configuration, one can find that the even plateaus of the conductance shrink, while the odd ones almost remain unchanged [Fig. 5(a)]. These characteristic phenomena also stem from the combined effect of the spin-selective scattering, the Zeeman splitting of the subbands in the two FM electrodes, and the increase of the separation between the subbands with increasing the strain strength [see Fig. 2(b)].

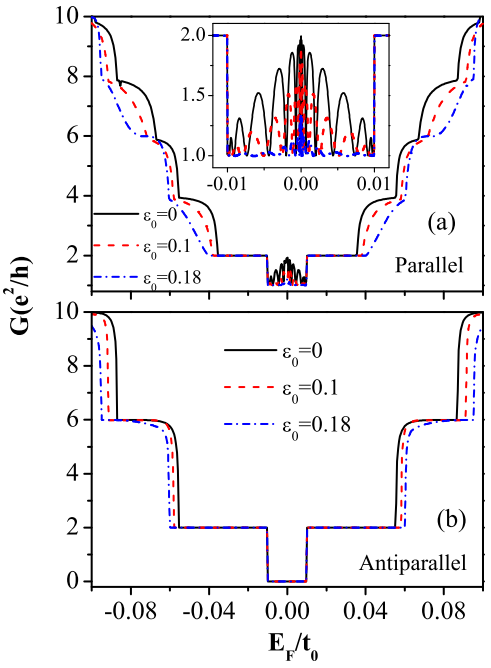

FIG. 5. (Color online) The conductance as a function of Fermi energy at ε_0 and $\theta = 0$ for (a) parallel and (b) antiparallel configurations of magnetization of two ferromagnetic electrodes. The inset in (a) shows the low energy region more clearly. The other parameters are taken the same as the those of Fig. 3.

V. STRAIN INDUCED TRANSITION OF MAGNETORESISTANCE

Under the uniaxial strain, the MR is found to reveal a transition behavior. Figure 6 shows the Fermi energy dependence of the MR for different strain strength ε_0. No strain, the MR versus the Fermi energy exhibits a perfect histogramlike structure, which is symmetric with respect to the zero energy. When the strain plays a role, the plateau of the MR around the origin is not changed at all. However, the other histogramlike peaks of the MR start to shrink upon the application of the parallel strain, and finally develop into successive cusplike peaks for a sufficiently large strain, as seen in Fig. 6(a). Owing to the combined effect of the spin-dependent scattering and the strain, the width of each plateau in the conductance becomes larger for a stronger parallel strain in the antiparallel configuration. As a comparison, for parallel configuration, the even (odd) plateaus diminish (remain unchanged) with increasing the longitudinal strain strength [see Figs. 5(a) and 5(b)].

In contrast, when the transverse strain ($\theta = \pi/2$) is applied, the concavity between the MR histogramlike peaks promptly shrinks, and rises with larger strain, as shown in Fig. 6(b). In particular, as the strain strength grows to an appropriate value, the concavities arrive at the values of the corresponding plateaus so that the MR as a function of the Fermi energy exhibits a successive steplike structure. Furthermore, a larger strain even causes the concavity to go into a sharp peak located at the edge of the plateau. This behavior is also related to the fact that the plateau width of the conductance versus the strain strength are quite different for the parallel and antiparallel configurations.

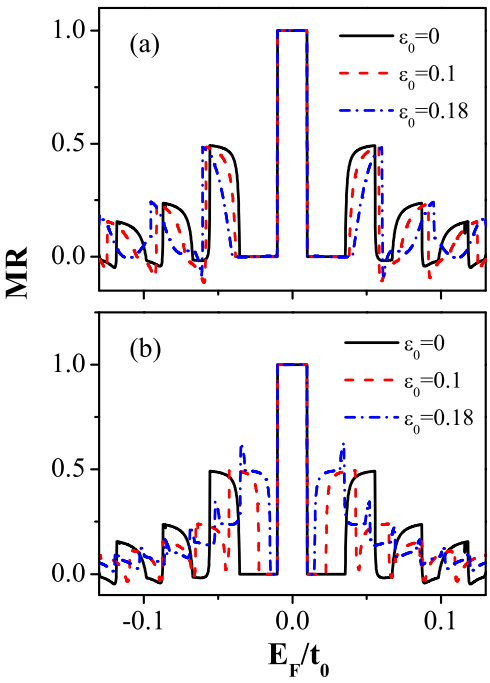

FIG. 6. (Color online) The magnetoresistance as a function of Fermi energy for different ε_0 at (a) $\theta = 0$ and (b) $\theta = \pi/2$. The other parameters are taken the same as those of Fig. 3.

VI. CURRENT-INDUCED SPIN TRANSFER TORQUE

In this section we investigate the CISTT in the strained graphene spin-valve device. According to Eq. (11), for a small bias voltage V, the CISTT per unit of the bias voltage at zero temperature is expressed as

$$\frac{\tau^{Rx}}{V} = \frac{e}{4\pi}\mathrm{Tr}\{[G^r(E_F)\Gamma_L(E_F)G^a(E_F)\Gamma_R(E_F)] \times (\sigma_x \cos\varphi - \sigma_z \sin\varphi)\}.$$

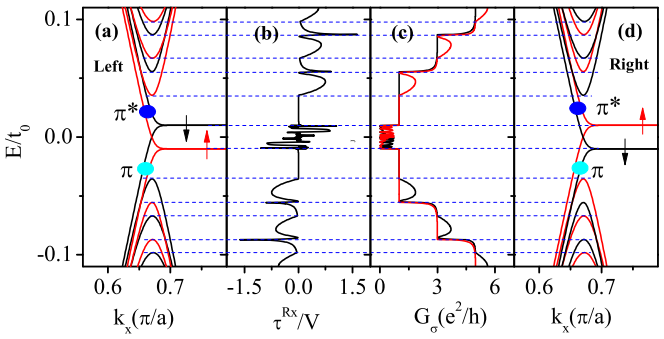

FIG. 7. (Color online) The CISTT per unit of the bias voltage V in unit of $e/4\pi$ (b) and the conductance of each spin direction (c) as a function of Fermi energy in the absence of a strain. The corresponding band structures of the left and right spin-polarized ZGNR electrodes are also presented in (a) for $\varphi = 0$ and (d) for $\varphi = 2\pi/3$, respectively. The arrows indicate the spin directions of electrons in the ferromagnetic electrodes. The other parameters are taken the same as those of Fig. 3.

Figure 7(b) shows the CISTT per unit of the bias voltage as a function of Fermi energy in the absence of strain. In order to elucidate the dependence of the CISTT on the Fermi energy, we also plot the conductance of each spin component versus the Fermi energy in Fig. 7(c) as well as the corresponding band structures of two electrodes in Figs. 7(a) and 7(d). The CISTT in the magnetic tunneling junctions is proportional to $\mathbf{S}_R\times(\mathbf{S}_L\times\mathbf{S}_R)$ [33], where $\mathbf{S}_L$ and $\mathbf{S}_R$ are the spin moments in the left and right ferromagnetic electrodes. For the graphene spin-valve device, when replacing E_F by $-E_F, \mathbf{S}_{L,R}=-\mathbf{S}_{L,R}$ due to the electron-hole symmetry, thus, one can observe that τ^{Rx}/V versus the Fermi energy is inversion symmetrical to the axis of $E_F=0$ [see Fig. 7(b)]. Here we only discuss the case of $E_F>0$, for which the curve of τ^{Rx}/V versus E_F can be partitioned into several regions: $(0,M)$, $(M,E^p_{1\uparrow})$, and $(E^p_{n-1\uparrow},E^p_{n\uparrow})$, where $n\geqslant 2$. In the region $E_F\in(0,M)$, τ^{Rx}/V exhibits an oscillation behavior, which is related to the combined effect of the band filter and spin-dependent scattering. When continuously increasing E_F to the interval $(M,E^p_{1\uparrow})$, the τ^{Rx}/V forms a zero value plateau whose width is equal to $E^p_{1\uparrow}-M$. In this region, the spin-up and spin-down currents are equal to each other, leading to zero CISTT [see Figs. 7(a), 7(c), and 7(d)]. When $E_F\in(E^p_{n-1\uparrow},E^p_{n\uparrow})$, τ^{Rx}/V develops a broad peak closely followed by a sharp one. This behavior can be accounted for by considering the dependence of the conductance G_σ for each spin direction on the Fermi energy. In the interval $E_F\in(E^p_{n\uparrow},E^p_{n\downarrow})$, the spin-up conductance starts to rise followed by a decrease, forming a broad peak; however the spin-down conductance still remains intact [see Fig. 7(c)]. When E_F approaches $E^p_{n\downarrow}$, the spin-up and spin-down conductances dramatically increase to a new plateau. The subtle difference between the spin-up and spin-down conductances in the region $(E^p_{n\uparrow},E^p_{n\downarrow})$ reflects the observed characteristic features in τ^{Rx}/V versus E_F.

When the longitudinal stain is applied, Fig. 8(b) shows the dependence of τ^{Rx}/V on the Fermi energy for different strain strength ε_0. With increasing the ε_0, the positions of the broad peaks and the sharp peaks are moved to higher energy. And, it is interesting to note that the amplitude and width of each broad peak of the τ^{Rx}/V versus E_F shrink monotonously. However, there exists a threshold strain strength ε_c for the sharp peaks. When $\varepsilon_0<\varepsilon_c$, the sharp peaks increase with increasing ε_0; while for $\varepsilon_0>\varepsilon_c$ they are suppressed by the strain. Moreover, ε_c becomes larger for the sharp peaks at higher energies. We assign these behaviors to the result of a nontrivial combined effect of the strain and the spin-dependent scattering in the graphene spin-valve device, which will become clear when taking into account the dependence of the spin conductance on the Fermi energy for different ε_0. In the presence of such a longitudinal strain, the bonds t_1,t_3 between the nearest neighbor carbons are suppressed, and the scattering experienced by the transported electrons strongly depends on the spin orientation. One can observe that for the spin-up electrons, the amplitudes and width of the broad peaks of the conductance always decay with the applied strain. While for the spin-down electrons the plateau values of the conductance remains unchanged, as shown Fig. 8(a). In particular, the edges of the second plateaus of the spin-up and spin-down

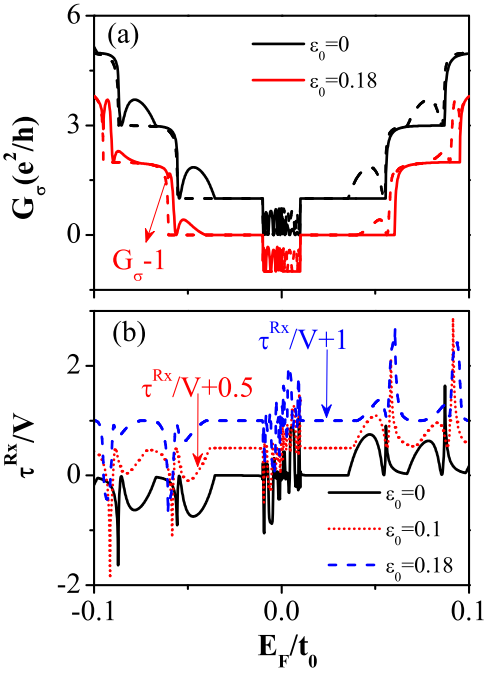

FIG. 8. (Color online) (a) The conductance of each spin direction and (b) the CISTT per unit of the bias voltage V in unit of $e/4\pi$ as a function of Fermi energy for different ε_0. The solid and dash lines in (a) correspond to the spin-down and spin-up conductances, respectively. The angle between the magnetizations of the left and right ferromagnetic leads is $\varphi=\pi/3$. The other parameters are taken the same as those of Fig. 3.

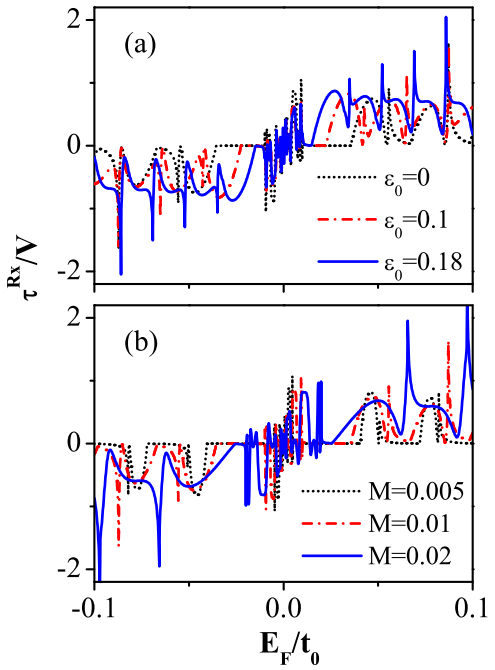

FIG. 9. (Color online) The CISTT per unit of the bias voltage V in unit of $e/4\pi$ as a function of Fermi energy (a) for different ε_0 at $\theta=\pi/2, M=0.01$, and (b) for different M at $\varepsilon_0=0$. $\varphi=\pi/3$ is set for the curves in both (a) and (b). The other parameters are taken the same as those of Fig. 3.

conductances do not coincide with each other. Furthermore, this disparity is further enhanced for the plateau located at higher energy, which is the origin of the observed features.

Figure 9 shows τ^{Rx}/V as a function of E_F for different transverse strain strength in (a) and magnetization in (b), respectively. It is found that more (less) peaks appear in a same Fermi energy region with enhancing the strain strength (magnetization). This is apparently the consequence of the variation of the subbands' distance affected by varying the strain and the magnetization. Another observation is that the sharp peaks become more prominent and sharpened with a stronger strain and larger magnetization. Since the sharp peaks are induced by a difference between spin-up and spin-down conductances at the edge of the conductance plateau, this indicates a larger spin splitting at the edge consistent with the results of the previous section.

VII. SUMMARY

In summary, based on the nonequilibrium Green's function method, we investigated theoretically the spin-dependent transport through a zigzag-edged-graphene-nanoribbon-based spin-valve device in the presence of a uniaxial strain acting to the graphene sheet. Our results show that the shapes and the separation of subbands of the ZGNR are strongly governed by the strain strength and the tensile direction. When the longitudinal or transverse strain is applied, the conductance around the Dirac point ($E_F = 0$) remains intact. However, for the Fermi energy larger than the magnetization of the electrodes, the width of each plateau of the conductance increases (decreases) with increasing the longitudinal (transverse) strain strength for the antiparallel configuration. In contrast, for the parallel configuration, the even (odd) plateaus of the conductance shrink, while the odd (even) ones almost remain unchanged for the longitudinal (transverse) strain. Correspondingly, this may lead to a transition of the MR from a perfect histogramlike behavior to a successive cusplike-peak behavior when the longitudinal strain is applied, or to a steplike behavior with sharp peaks when the transverse strain is applied. It is also shown that the CISTT per unit of the bias voltage as a function of the Fermi energy exhibits successive oscillations of broad peaks closely followed by sharp ones, which results from the cooperated effect of the strain and spin-dependent scattering.

ACKNOWLEDGMENTS

The work was supported in part by the Natural Science Foundation of China (Grant No. 10904007), the MOST (No. 2012CB932901, No. 2013CB933401), the Strategic Priority Research Program of the Chinese Academy of Sciences, Grant No. XDB07010100, the Scientific Research Fund of Hunan Provincial Education Department (Grant No. 13A109), Aid Program for Science and Technology Innovative Research Team in Higher Educational Institutions of Hunan Province, and the Construct Program of the Key Discipline of Hunan Province, China. Z. G. Zhu is supported by Hundred Talents Program of the Chinese Academy of Sciences and by Scientific Research Equipment Project of the Chinese Academy of Sciences.

[1] K. S. Novoselov, A. K. Geim, S. V. Morozov, D. Jiang, Y. Zhang, S. V. Dubonos, I. V. Grigorieva, and A. A. Firsov, Science **306**, 666 (2004).
[2] K. S. Novoselov, A. K. Geim, S. V. Morozov, D. Jiang, M. I. Katsnelson, I. V. Grigorieva, S. V. Dubonos, and A. A. Firsov, Nature (London) **438**, 197 (2005).
[3] Y. Zhang, Y. W. Tan, H. L. Stormer, and P. Kim, Nature (London) **438**, 201 (2005).
[4] K. I. Bolotin, K. J. Sikes, Z. Jiang, G. Fudenberg, J. Hone, P. Kim, and H. L. Stormer, Solid State Commun. **146**, 351 (2008).
[5] N. Tombros, C. Jozsa, M. Popinciue, H. T. Jonkman, and B. J. Van Wees, Nature (London) **448**, 571 (2007).
[6] S. A. Wolf *et al.*, Science **294**, 1488 (2001); I. Žutić *et al.*, Rev. Mod. Phys. **76**, 323 (2004); J. Fabian *et al.*, Acta Phys. Slovaca **57**, 565 (2007); P. Seneor *et al.*, MRS Bull. **37**, 1245 (2012); Z.-G. Zhu and G. Su, Sci. China-Phys. Mech. Astron. **56**, 166 (2013).
[7] S. Cho, Y. F. Chen, and M. S. Fuhrer, Appl. Phys. Lett. **91**, 123105 (2007).
[8] M. Ohishi, M. Shiraishi, R. Nouchi, T. Nozaki, T. Shinjo, and Y. Suzuki, Jpn. J. Appl. Phys. **46**, L605 (2007).
[9] W. H. Wang, K. Pi, Y. Li, Y. F. Chiang, P. Wei, J. Shi, and R. K. Kawakami, Phys. Rev. B **77**, 020402(R) (2008).
[10] K. H. Ding, Z. G. Zhu, and J. Berakdar, Phys. Rev. B **79**, 045405 (2009).
[11] J. C. Chen, S. G. Cheng, S. Q. Shen, and Q. F. Sun, J. Phys.: Condens. Matter **22**, 035301 (2010).
[12] H. Cheraghchi and F. Adinehvand, J. Phys.: Condens. Matter **24**, 045303 (2012).
[13] B. Zhou, X. Chen, H. Wang, K. H. Ding, and G. Zhou1, J. Phys.: Condens. Matter **22**, 445302 (2010).
[14] W. Sheng, Z. Y. Ning, Z. Q. Yang, and H. Guo, Nanotechnology **21**, 385201 (2010).
[15] J. Kang, F. Wu, and J. Li, Appl. Phys. Lett. **98**, 083109 (2011).
[16] H.-X. Yang, A. Hallal, D. Terrade, X. Waintal, S. Roche, and M. Chshiev, Phys. Rev. Lett. **110**, 046603 (2013).
[17] A. H. Castro Neto, F. Guinea, N. M. R. Peres, K. S. Novoselov, and A. K. Geim, Rev. Mod. Phys. **81**, 109 (2009).
[18] F. Guinea, M. I. Katsnelson, and A. K. Geim, Nat. Phys. **6**, 30 (2010).
[19] F. Guinea, A. K. Geim, M. I. Katsnelson, and K. S. Novoselov, Phys. Rev. B **81**, 035408 (2010).
[20] T. Low and F. Guinea, Nano Lett. **10**, 3551 (2010).
[21] M. Neek-Amal and F. M. Peeters, Phys. Rev. B **85**, 195446 (2012).
[22] V. M. Pereira, R. M. Ribeiro, N. M. R. Peres, and A. H. Castro Neto, Europhys. Lett. **92**, 67001 (2010).
[23] F. M. D. Pellegrino, G. G. N. Angilella, and R. Pucci, Phys. Rev. B **81**, 035411 (2010).
[24] M. G. Xia and S. L. Zhang, Eur. Phys. J. B **84**, 385 (2011).

[25] F. M. D. Pellegrino, G. G. N. Angilella, and R. Pucci, J. Phys.: Conf. Ser. **377**, 012083 (2012).
[26] H. Haug and A. P. Jauho, *Quantum Kinetics in Transport and Optics of Semiconductors* (Springer, Berlin, 1998).
[27] J. Rammer, *Quantum Transport Theory* (Westview, Boulder, CO, 2004).
[28] V. M. Pereira, A. H. Castro Neto, and N. M. R. Peres, Phys. Rev. B **80**, 045401 (2009).
[29] Q. F. Sun and X. C. Xie, Phys. Rev. Lett. **104**, 066805 (2010).
[30] D. H. Lee and J. D. Joannopoulos, Phys. Rev. B **23**, 4997 (1981).
[31] M. P. L. Sancho, J. M. L. Sancho, and J. Rubio, J. Phys. F: Met. Phys. **15**, 851 (1985).
[32] J. C. Slonczewski, Phys. Rev. B **39**, 6995 (1989).
[33] Z. G. Zhu, G. Su, B. Jin, and Q. R. Zheng, Phys. Lett. A **306**, 249 (2003).
[34] H. F. Mu, G. Su, and Q. R. Zheng, Phys. Rev. B **73**, 054414 (2006).
[35] K. Nakada, M. Fujita, G. Dresselhaus, and M. S. Dresselhaus, Phys. Rev. B **54**, 17954 (1996).
[36] K. Wakabayashi, K. Sasaki, T. Nakanishi, and T. Enoki, Sci. Technol. Adv. Mater. **11**, 054504 (2010).
[37] W. Y. Kim and K. S. Kim, Nat. Nanotech. **3**, 408 (2008).
[38] Q. Yue, S. Chang, J. Tan, S. Qin, J. Kang, and J. Li, Phys. Rev. B **86**, 235448 (2012).
[39] The subbands for $E \geqslant 0$ ($E < 0$) are labeled by the integers $n \geqslant 0$ ($n < 0$). Since the conductance obeys the electron-hole symmetry, i.e., $G(-E_F) = G(E_F)$, here we only discuss the case of $n \geqslant 0$ which is valid for that of $n < 0$.